nature geoscience

LETTERS

PUBLISHED ONLINE: 31 JULY 2011 | DOI: 10.1038/NGEO1213

Superficial simplicity of the 2010 El Mayor–Cucapah earthquake of Baja California in Mexico

Shengji Wei[1]*, Eric Fielding[2], Sebastien Leprince[1], Anthony Sladen[1,3], Jean-Philippe Avouac[1], Don Helmberger[1], Egill Hauksson[1], Risheng Chu[1], Mark Simons[1], Kenneth Hudnut[1,4], Thomas Herring[5] and Richard Briggs[6]

The geometry of faults is usually thought to be more complicated at the surface than at depth and to control the initiation, propagation and arrest of seismic ruptures[1–6]. The fault system that runs from southern California into Mexico is a simple strike-slip boundary: the west side of California and Mexico moves northwards with respect to the east. However, the M_w 7.2 2010 El Mayor–Cucapah earthquake on this fault system produced a pattern of seismic waves that indicates a far more complex source than slip on a planar strike-slip fault[7]. Here we use geodetic, remote-sensing and seismological data to reconstruct the fault geometry and history of slip during this earthquake. We find that the earthquake produced a straight 120-km-long fault trace that cut through the Cucapah mountain range and across the Colorado River delta. However, at depth, the fault is made up of two different segments connected by a small extensional fault. Both segments strike N130° E, but dip in opposite directions. The earthquake was initiated on the connecting extensional fault and 15 s later ruptured the two main segments with dominantly strike-slip motion. We show that complexities in the fault geometry at depth explain well the complex pattern of radiated seismic waves. We conclude that the location and detailed characteristics of the earthquake could not have been anticipated on the basis of observations of surface geology alone.

The El Mayor–Cucapah earthquake that occurred on 4 April 2010 produced extensive liquefaction in the Colorado River delta area and in the Mexicali and Imperial valleys, and numerous rockfalls occurred in the Sierra Cucapah. This is the largest earthquake to have struck the southern California and northern Baja California, Mexico area since the M_w 7.3 Landers earthquake of 1992 (ref. 8). The GCMT (global centroid moment tensor) of the mainshock reveals a double-couple component corresponding to a scalar moment of 7.28×10^{19} N m (M_w 7.17), with a significant non-double-couple (CLVD) component (2.4×10^{19} N m; Fig. 1; ref. 7). The mainshock occurred where the system of continental parallel right-lateral strike-slip faults including the San Andreas, San Jacinto and Elsinore faults connect with a system of transform faults and active spreading centres in the Gulf of California to the south[9] (Fig. 1 and Supplementary Fig. S1). This fault system forms the plate boundary in southern California, where the Pacific plate moves northwestwards with respect to North America at about 46 mm yr^{-1} (Fig. 1, inset). The main active fault recognized in the area was the Laguna Salada fault, a right-lateral normal oblique fault bounding the Sierra Cucapah to the west. It accommodated a M_w 7.1 earthquake in 1892 (ref. 10; Supplementary Fig. S1).

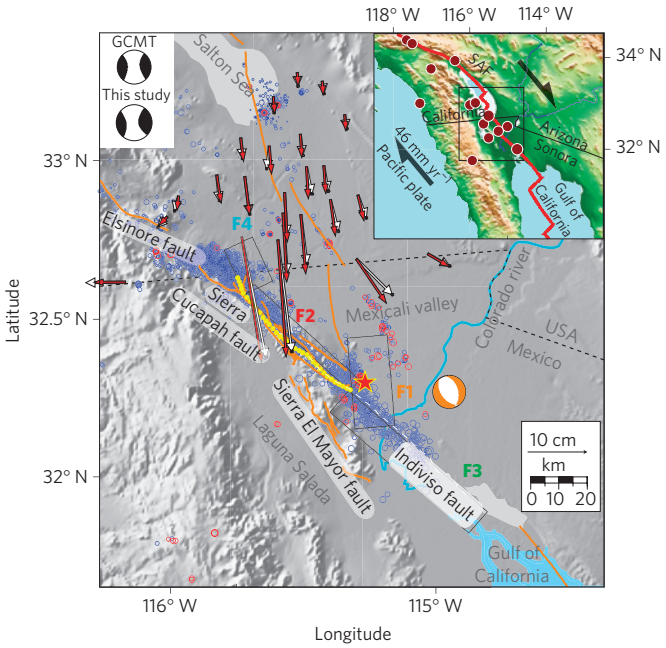

Figure 1 | Setting of the El Mayor–Cucapah earthquake. The inset shows historical $M > 6.5$ earthquakes (red circles) and a simplified plate boundary (red line). Yellow and white circles denote surface ruptures determined from correlation of optical and SAR images. Circles show seismicity ($M > 2.5$) 4 months before (red) and 11 days after (blue) the earthquake, relocated with the double-difference method[18]. Left top corner, moment tensor derived from this study and GCMT. Labelled rectangles show the fault geometry used in the inversion. The focal mechanism derived from the first 15 s of teleseismic P-waves is shown in orange, with the epicentre reported as the red star. Arrows show horizontal coseismic displacements measured at PBO GPS stations (data in white, with 95% confidence ellipses, and synthetic in red). SAF, San Andreas fault.

We synthesize the earthquake data using modern methods in seismology, tectonic geodesy and remote sensing (global

[1]Division of Geological and Planetary Sciences, California Institute of Technology, Pasadena, California 91125, USA, [2]Jet Propulsion Laboratory, California Institute of Technology, Pasadena, California 91109, USA, [3]Geoazur, Observatoire de la Côte d'Azur, Université de Nice-Sophia Antipolis, CNRS, IRD, Valbonne, 06103 Nice Cedex 2, France, [4]United States Geological Survey, Pasadena, California 91106, USA, [5]Department of Earth, Atmospheric, and Planetary Sciences, Massachusetts Institute of Technology, Cambridge, Massachusetts 02139, USA, [6]United States Geological Survey, Golden, Colorado 80401, USA. *e-mail: shjwei@caltech.edu.

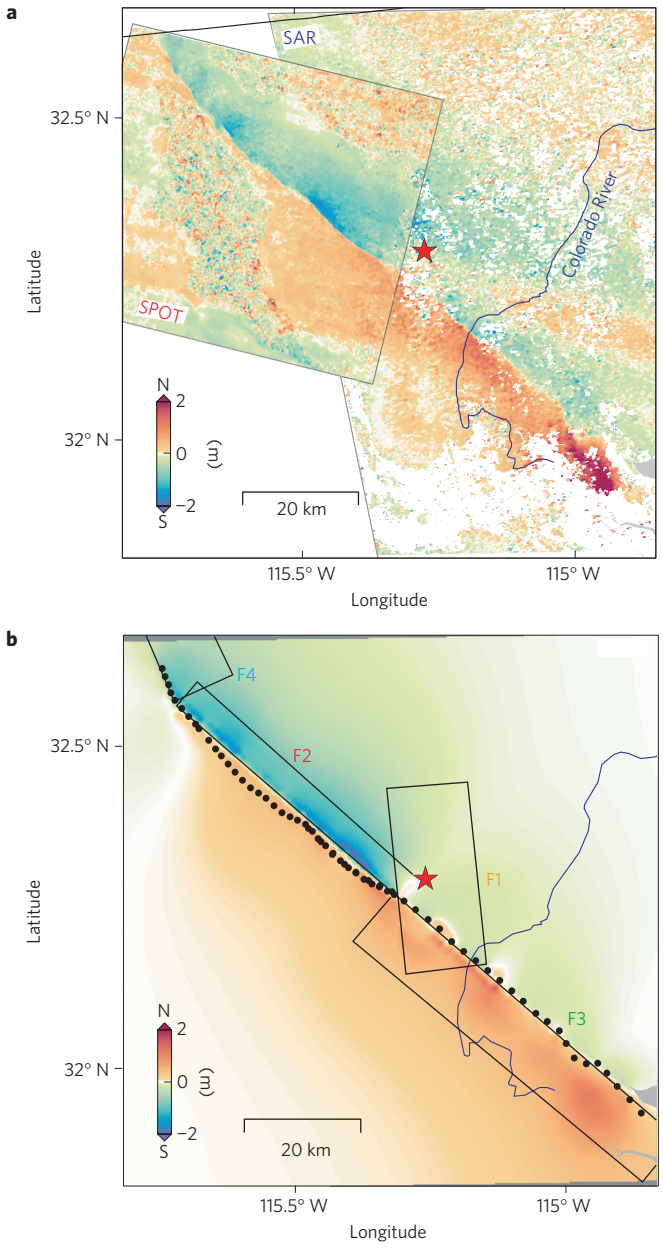

Figure 2 | North–south surface displacements measured from subpixel correlation of optical and SAR images. a, Map of near-field coseismic ground displacement measured from subpixel correlation of SAR amplitude images[25] and optical SPOT images[26,27] acquired before and after the earthquake. The SPOT measurements are over-printing the SAR azimuth offsets. **b**, Prediction from the preferred model. The colour scale is blue (respectively, red) for southward (respectively, northward) displacements. The red star shows the location of the epicentre. The black dots delineate the fault trace as determined from the SAR and optical image correlations. The thin black rectangles show the idealized fault segments used in the modelling.

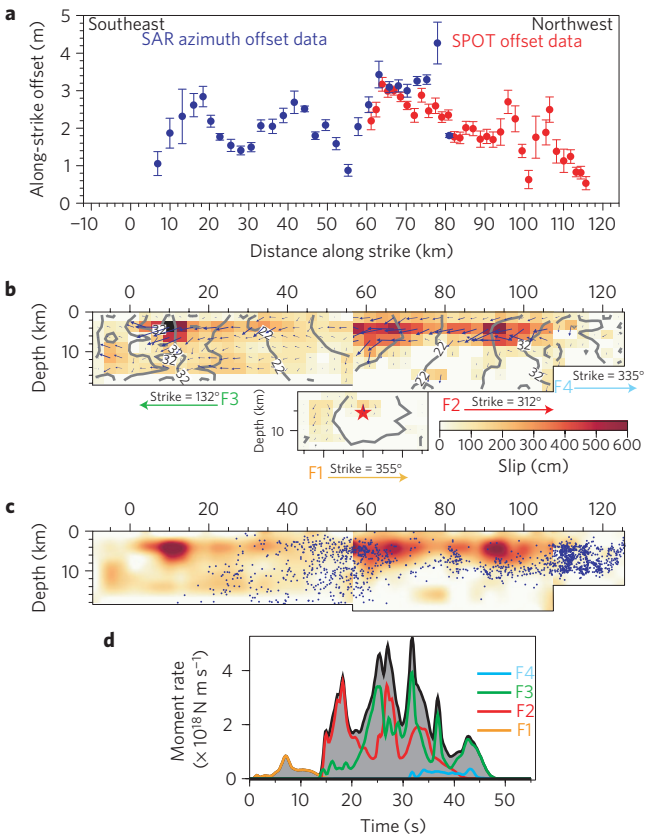

Figure 3 | Slip distribution and rupture history. a, Surface slip measured from serial profiles across the fault trace based on the SAR (blue) and SPOT (red) images. **b**, Cumulative slip (arrows show slip vectors, and colour coding shows amplitude) and isochrons of the seismic rupture. The rupture times are given relative to the onset of slip at the epicentre. Note the large displacements around 17 and 27 s on F2. **c**, Comparison of relocated aftershocks projected on the faults with slip distribution (smoothed). **d**, Source time function showing the time evolution of released moment rate. The contribution of each fault segment is colour coded.

positioning systems (GPS), interferometric synthetic aperture radar (InSAR), subpixel correlation of optical satellite images, and synthetic aperture radar (SAR)). See the Supplementary Information for details on data and methods. The remote-sensing data reveal an almost linear and continuous fault trace extending over about 120 km from the northern tip of the Sierra Cucapah to the Gulf of California, with right-lateral slip of about 2 m on average (Fig. 1). These data indicate that the 4 April 2010 mainshock did not rupture the Laguna Salada fault but rather two other faults, the Borrego and Pescadores faults within the Sierra Cucapah, which had been mapped but not recognized to be active[10] (Supplementary Fig. S1). Our data also reveal a major strike-slip segment that extends from the epicentre to the southeast, across the Colorado River delta. This part of the mainshock rupture, which has been verified in the field and named the Indiviso fault[11], occurred along basement faults beneath the sedimentary deposits of the Colorado River. Thus, the southeast surface trace does not coincide with previously identified active faults having obvious geomorphic expression, such as the Laguna Salada fault or the Cañada David detachment. Rather, the earthquake ruptured along a complex set of existing, less active faults, illustrating the ongoing process by which the slip along the Elsinore fault connects to the transform plate boundary in the Gulf of California.

Overall, the location and focal mechanism of the earthquake are consistent with right-lateral slip along the right-lateral transform plate boundary fault system (Fig. 1). However, the large non-double-couple component of the moment tensor indicates a substantial component of normal faulting. The modelling of the first 15 s of the teleseismic waveforms (Supplementary Fig. S2) indicates that the earthquake actually initiated as a normal event (Fig. 1). This observation, together with the clear asymmetry of surface strain seen from the correlation of the optical (SPOT)

Table 1 | Moment tensor solutions of GCMT and this study.

	M_{rr}	M_{tt}	M_{pp}	M_{rt}	M_{rp}	M_{tp}	M_0	M_{DC}	M_{CLVD}	Unit (N m)
GCMT	−2.49	−5.94	8.43	0.56	−0.14	−0.86		7.28	2.84	10^{19}
Static inversion	−1.42	−6.42	7.84	0.11	−1.05	−1.55	9.91	7.50	2.11	10^{19}
Joint inversion	−2.03	−6.07	8.10	−0.23	−1.28	−1.62	9.90	7.36	2.14	10^{19}

The moment tensor solution for the finite-fault slip models is obtained by summing up the contributions of each subfault. M_{rr}, M_{tt}, M_{pp}, M_{rt}, M_{rp} and M_{tp} are the six moment tensor (symmetric) components, M_0 is the total moment, M_{DC} is the best double-couple moment and M_{CLVD} is the moment of the compensated linear vector dipole.

and SAR images (Japanese Aerospace Exploration Agency ALOS PALSAR) as well as from InSAR analysis of PALSAR and European Space Agency Envisat ASAR data (see Supplementary Information), requires a complex fault geometry at depth that seems at odds with the relatively straight strike-slip fault trace observed at the surface (Fig. 2).

We use finite-fault source modelling to determine what geometry and slip distribution reconcile all of the observations gathered in this study. We discretized the rupture zone into slipping patches (point sources) that contribute to the wave field at a particular time controlled by the rupture velocity and rise time[12]. Trade-offs among the amplitude of slip, the rupture velocity and the rise time[13,14] are limited because constraints on the fault geometry are provided by the remote-sensing observations. We concentrate on geometrical fault irregularities that can influence large events[4] but are not easily resolved by seismology alone. We built the simplest possible fault geometry required to fit our observations. We chose a N355° E-striking fault plane dipping 45° to the east (F1) to account for the teleseismic waveforms (Supplementary Fig. S2) and to match the local alignment of aftershocks near the epicentre. We defined a relatively large fault plane (33 km long), consistent with the 15 s duration of the first sub-event. Segments F2 (51 km long, striking N312° E), F3 (60 km long, striking N132° E) and F4 (18 km long, striking N335° E) were defined to follow the surface traces. We use the geodetic and InSAR data to determine the best-fitting dip angles based on 5° grid-search steps. The best dip angles are 75° to the east for F2, 60° to the west for F3, and 50° to the east for F4. The GPS data (presented as vectors in Fig. 1) are recorded by Plate Boundary Observatory (PBO) stations located in the US. These are closest to the northern segment, and constrain the dip angle of F4. The dip angles of F2 and F3 are mostly controlled by the InSAR data (see Supplementary Information for details). Although the fault must be more complex at a finer scale and shallow depths, we are able to explain the bulk of our combined data sets with these four segments.

To generate the kinematic model, we invert for the distribution of slip in terms of rake direction, amplitude of slip, rupture velocity and rise time[15]. Using the geodetic data (GPS and remote sensing), we first determine a static coseismic slip model representing the cumulative slip distribution due to the earthquake (Supplementary Fig. S3). We use the horizontal offsets measured from the SAR and SPOT images to constrain the fault slip at the surface (Fig. 2a), and the whole geodetic and InSAR data set to constrain the static displacement field. As a result of the simplified fault geometry, the formal inversion of shallow slip would indeed be biased to lower slip wherever the fault model does not follow exactly the measured fault trace. To avoid this bias, we impose slip on the shallow portion of the fault to fit the horizontal surface slip measured from the SAR and SPOT images to within the average 2 σ uncertainty on these measurements (±0.5 m; Fig. 3a; ref. 16). To restrict the large number of data points to be inverted, we resample the unwrapped interferograms[17] (Supplementary Figs S4–S6), and carry out the inversion for a static solution (Supplementary Fig. S3). This model is then used to estimate the entire surface deformation field and assess residuals (Supplementary Figs S8–S11). A model compatible with all of the static data is shown in Fig. 2b. North of the epicentre, the motion on the northeastern side of the surface trace (blue) is larger than that (red) on the southwest. This asymmetry is clear evidence that faults F2 and F3 are dipping in opposite directions (see Supplementary Figs S4–S11 for modelling details).

To determine the time evolution of the rupture, we jointly inverted the seismological and geodetic data (remote sensing and GPS). The model is parameterized in terms of the distribution of slip (characterized by rake and amplitude of slip at each node), the rupture velocity and the rise time[15]. Regularization of the slip inversions was through a penalty factor applied to Laplacian smoothing of the slip distribution (Supplementary Fig. S12).

The static or total slip distribution of the model obtained from the joint inversion of the geodetic, remote-sensing and seismological data (Fig. 3b) is very close to the solution obtained from the inversion of the static deformation data (Supplementary Fig. S3). The only difference is that slip on F1 cannot be constrained from the geodetic data and is better determined from the seismological data. The total moment of the joint inversion model is 9.9×10^{19} N m, which is calculated by summing up the contribution of each subfault. The moment tensor is actually very close to the GCMT solution[7] (Table 1). The double-couple moment is 7.4×10^{19} N m and the CLVD component is 2.1×10^{19} N m. This model provides a remarkably good fit to the seismological data (Supplementary Figs S13 and S14), demonstrating the internal consistency of the whole data set.

Overall, most of the energy release occurred at depths of less than 9 km, with slip reaching up to 6 m. The inferred rupture velocity is quite variable and relatively low, about 2.5 km s^{-1} on average. The moment release history reflects the successive rupture of different asperities on faults F1 to F4 (zones with locally high seismic slip) whose location is essentially constrained by the geodetic data (Fig. 3). The earthquake started with a dominantly normal sub-event on F1. This sub-event was not very impulsive, with most of the moment release over about 8 s, which is a relatively long duration for an M_w 6.3 earthquake. There was an even smaller event a few seconds earlier, which can be seen in some teleseismic waveforms (Supplementary Fig. S14). The event on F1 triggered rupture of segments F2 to the north and F3 to the south; F2 produced a sharp pulse of moment release 17–27 s after the onset of the rupture (Fig. 3d and Supplementary Fig. S15). The peak in the moment release rate occurred at around 27 s, when the rupture reached nearly simultaneously the high slip patches on F2 and F3. Altogether the rupture lasted about 45–50 s.

The distributions of coseismic slip and relocated aftershocks[18] indicate that the seismogenic zone extends to depths of only about 10 km (Fig. 3c). The depth extent is probably limited by the high crustal temperature in this zone of tectonic transition from spreading centres and transform faults in the Gulf of California to continental faulting along the San Andreas fault system to the north[19]. The distribution of aftershocks is clearly anti-correlated with coseismic slip, especially north of the epicentre, where the hypocentral depth of aftershocks and the coseismic slip distribution are better constrained (Fig. 3c). Such an anti-correlation has been observed in a number of previous studies[20–23], indicating that

some of the aftershocks release residual strains near the patches of high slip.

The mainshock started as a moderate sub-event and evolved only ~15 s later into a more significant event (Fig. 3d). This rupture behaviour challenges the idea that the final size of large earthquakes can be predicted within seconds of the onset of rupture[24]. The mainshock initiated at a local structural complexity owing an extensional jog at depth (defined by F1) between faults F2 and F3 (Supplementary Fig. S16). More generally, the complex mainshock rupture illustrates how fault bends and jogs, not necessarily visible from the surficial fault trace geometry, influence the initiation, the evolution and the termination of earthquake ruptures[1–3,5]. The system of faults that ruptured in this event probably owes its geometric complexity to its immaturity, as the plate boundary is shifting to a new location linking the Elsinore fault to the Gulf of California.

Received 8 August 2010; accepted 23 June 2011; published online 31 July 2011

References

1. Bouchon, M., Campillo, M. & Cotton, F. Stress field associated with the rupture of the 1992 Landers, California, earthquake and its implications concerning the fault strength at the onset of the earthquake. *J. Geophys. Res.* **103,** 21091–21097 (1998).
2. Harris, R., Archuleta, R. & Day, S. Fault steps and the dynamic rupture process: 2-D numerical simulations of a spontaneously propagating shear fracture. *Geophys. Res. Lett.* **18,** 893–896 (1991).
3. King, G. C. & Nabelek, J. The role of fault bends in faults in the initiation and termination of earthquake rupture. *Science* **283,** 984–987 (1985).
4. Wesnousky, S. G. Predicting the endpoints of earthquake ruptures. *Nature* **444,** 358–360 (2006).
5. Wesnousky, S. G. Displacement and geometrical characteristics of earthquake surface ruptures: Issues and implications for seismic-hazard analysis and the process of earthquake rupture. *Bull. Seismol. Soc. Am.* **98,** 1609–1632 (2008).
6. Radiguet, M., Cotton, F., Manighetti, I., Campillo, M. & Douglas, J. Dependency of near-field ground motions on the structural maturity of the ruptured faults. *Bull. Seismol. Soc. Am.* **99,** 2572–2581 (2009).
7. http://www.globalcmt.org/CMTsearch.html.
8. Sieh, K. *et al.* Near-field investigations of the Landers earthquake sequence, April to July 1992. *Science* **260,** 171–176 (1993).
9. Atwater, T. & Stock, J. Pacific North America plate tectonics of the Neogene southwestern United States: An update. *Int. Geol. Rev.* **40,** 375–402 (1998).
10. Fletcher, J. M. & Spelz, R. M. Patterns of Quaternary deformation and rupture propagation associated with an active low-angle normal fault, Laguna Salada, Mexico: Evidence of a rolling hinge? *Geosphere* **5,** 385–407 (2009).
11. Gonzalez-Garcia, J. J. *et al.* Seismotectonics of the 2010 El Mayor Cucapah—Indiviso earthquake and its relation to seismic hazard in southern California. *AGU (Fall Meeting)* abstr. T53B-2117 (2010).
12. Hartzell, S. & Helmberger, D. V. Strong-motion modeling of the Imperial Valley earthquake of 1979. *Bull. Seismol. Soc. Am.* **72,** 571–596 (1982).
13. Ji, C., Helmberger, D. V., Song, T-R. A., Ma, K-F. & Wald, D. J. Slip distribution and tectonic implications of the 1999 Chi–Chi, Taiwan earthquake. *Geophys. Res. Lett.* **28,** 4379–4382 (2001).
14. Delouis, B., Giardini, D., Lundgren, P. & Salichon, J. Joint inversion of InSAR, GPS, teleseismic, and strong-motion data for the spatial and temporal distribution of earthquake slip: Application to the 1999 Izmit mainshock. *Bull. Seismol. Soc. Am.* **92,** 278–299 (2002).
15. Ji, C., Wald, D. & Helmberger, D. V. Source description of the 1999 Hector Mine, California earthquake, part I: Wavelet domain inversion theory and resolution analysis. *Bull. Seismol. Soc. Am.* **92,** 1192–1207 (2002).
16. Avouac, J. P., Ayoub, F., Leprince, S., Konca, O. & Helmberger, D. V. The 2005, M_w 7.6 Kashmir earthquake: Sub-pixel correlation of ASTER images and seismic waveforms analysis. *Earth Planet. Sci. Lett.* **249,** 514–528 (2006).
17. Lohman, R. B. & Simons, M. Some thoughts on the use of InSAR data to constrain models of surface deformation: Noise structure and data downsampling. *Geochem. Geophys. Geosyst.* **6,** Q01007 (2005).
18. Hauksson, E. *et al.* The 2010 Mw 7.2 El Mayor–Cucapah earthquake sequence, Baja California, Mexico and southernmost California, USA: Active seismotectonics along the Mexican Pacific margin. *Pure Appl. Geophys. Top. Issue: Geodyn. Mexican Pacific Margin*, doi:10.1007/s00024-010-0209-7 (2010).
19. Blanpied, M. L., Lockner, D. A. & Byerlee, J. D. Frictional slip of granite at hydrothermal conditions. *J. Geophys. Res.* **100,** 13045–13064 (1995).
20. Yagi, Y., Kikuchi, M. & Sagiya, T. Co-seismic slip, post-seismic slip and aftershocks associated with two large earthquakes in 1996 in Hyugia-nada, Japan. *Earth Planet. Space* **53,** 793–803 (2001).
21. Hsu, Y. J. *et al.* Frictional afterslip following the 2005 Nias-Simeulue earthquake, Sumatra. *Science* **312,** 1921–1926 (2006).
22. Sladen, A. *et al.* Source model of the 2007 M_w 8.0 Pisco, Peru earthquake: Implications for seismogenic behavior of subduction megathrusts. *J. Geophys. Res.* **115,** B02405 (2010).
23. Tilmann, F. J. *et al.* The updip seismic/aseismic transition of the Sumatra megathrust illuminated by aftershocks of the 2004 Aceh-Andaman and 2005 Nias events. *Geophys. J. Int.* **181,** 1261–1274 (2010).
24. Ellsworth, W. L. & Beroza, G. C. Seismic evidence for an earthquake nucleation phase. *Science* **268,** 851–855 (1995).
25. Michel, R., Avouac, J. P. & Taboury, J. Measuring near field coseismic displacements from SAR images: Application to the Landers earthquake. *Geophys. Res. Lett.* **26,** 3017–3020 (1999).
26. Van Puymbroeck, N., Michel, R., Binet, R., Avouac, J. P. & Taboury, J. Measuring earthquakes from optical satellite images. *Appl. Opt.* **39,** 3486–3494 (2000).
27. Leprince, S., Barbot, S., Ayoub, F. & Avouac, J. P. Automatic and precise orthorectification, coregistration, and subpixel correlation of satellite images, application to ground deformation measurements. *IEEE Trans. Geosci. Remote Sensing* **45,** 1529–1558 (2007).

Acknowledgements

This work was financially supported by NSF, USGS, the Gordon and Betty Moore Foundation, NASA and SCEC. Regional seismic data were provided by SCSN and RESNOM. The Incorporated Research Institutions for Seismology (IRIS) Data Management System (DMS) was used to access the Global Seismographic Network data. The GPS analyses were obtained from the Earthscope PBO data products system and UNAVCO. Optical data were provided by USGS. Envisat data are copyright 2009, 2010 ESA and were obtained from the WInSAR archive and the Group on Earth Observation Geohazards Supersite virtual archive. ALOS data are copyright METI, JAXA and were obtained from the Alaska Satellite Facility Level 1 Data Pool. Part of this research was carried out at the Jet Propulsion Laboratory, California Institute of Technology under contract with the National Aeronautics and Space Administration. We thank CICESE colleagues J. Gonzalez and J. Fletcher for their support and interest, and we thank J. Hollingsworth for his suggestions to improve the figures. This is Tectonics Observatory contribution #172. SCEC is funded by NSF Cooperative Agreement EAR-0529922 and USGS Cooperative Agreement 07HQAG0008.

Author contributions

S.W. carried out the modelling and edited the paper; E.F. carried out the InSAR and SAR processing and edited the paper; S.L. carried out the optical image and SAR cross-correlation processing; A.S. helped with the modelling and downsampled the InSAR and SAR data; J-P.A. conceived and supervised the research and editing of the paper; D.H. supervised the research and edited the paper; E.H. carried out relocation of aftershocks and foreshocks; R.C. carried out modelling of teleseismic data; M.S. provided InSAR data; K.H. edited the paper and provided geological interpretation; T.H. carried out the processing of GPS data; R.B. contributed to the tectonic interpretation.

Additional information

The authors declare no competing financial interests. Supplementary information accompanies this paper on www.nature.com/naturegeoscience. Reprints and permissions information is available online at http://www.nature.com/reprints. Correspondence and requests for materials should be addressed to S.W.